*Biochemistry* **2000,** *39,* 2517−2529

# Porphyrin Interactions with Wild-type and Mutant Mouse Ferrochelatase[†]

Ricardo Franco,[‡,§] Jian-Guo Ma,[||] Yi Lu,[||] Gloria C. Ferreira,[‡] and John A. Shelnutt*,[||]

*Department of Biochemistry and Molecular Biology, College of Medicine, Institute for Biomolecular Science and H. Lee Moffit Cancer Center and Research Institute, University of South Florida, Tampa, Florida 33612, and Biomolecular Materials and Interfaces Department, Sandia National Laboratories, Albuquerque, New Mexico 87185-1349, and Department of Chemistry, University of New Mexico, Albuquerque, New Mexico 87131*

*Received June 11, 1999; Revised Manuscript Received October 15, 1999*

ABSTRACT: Ferrochelatase (EC 4.99.1.1), the terminal enzyme of the heme biosynthetic pathway, catalyzes $Fe^{2+}$ chelation into protoporphyrin IX. Resonance Raman and UV−vis absorption spectroscopies of wild-type and engineered variants of murine ferrochelatase were used to examine the proposed structural mechanism for iron insertion into porphyrin. The recombinant variants (i.e., H207N and E287Q) are enzymes in which the conserved amino acids histidine-207 and glutamate-287 of murine ferrochelatase were substituted with asparagine and glutamine, respectively. Both of these residues are at the active site of the enzyme as deduced from the *Bacillus subtilis* ferrochelatase three-dimensional structure. On the basis of changes in the UV−vis absorption spectrum, addition of free-base or metalated porphyrins to wild-type ferrochelatase and H207N variant yields a 1:1 complex, most likely a monomeric protein-bound species at the active site. In contrast, the addition of porphyrin (either free base or metalated) to E287Q is substoichiometric, as this variant retains bound porphyrin in the active site during isolation and purification. The specificity of porphyrin binding is confirmed by the narrowing of the structure-sensitive lines and the vinyl vibrational mode in the resonance Raman spectra. Shifts in the resonance Raman lines of free-base and metalated porphyrins bound to the wild-type ferrochelatase indicate a nonplanar distortion of the porphyrin macrocycle. However, the magnitude of the distortion cannot be determined without first defining the specific type of deformation. Significantly, the extent of the nonplanar distortion varies in the case of H207N- and E287Q-bound porphyrins. In fact, resonance Raman spectral decompositions indicate a homogeneous ruffled deformation for the nickel protoporphyrin bound to the wild-type ferrochelatase, whereas both planar and ruffled conformations are present for the H207N-bound porphyrin. Perhaps more revealing is the unusual resonance Raman spectrum of the endogenous E287Q-bound porphyrin, which has the structure-sensitive lines greatly upshifted relative to those of the free-base protoporphyrin in solution. This could be interpreted as an equilibrium between protein conformers, one of which favors a highly distorted porphyrin macrocycle. Taken together, these findings suggest that distortion occurs in murine ferrochelatase for some porphyrins, even without metal binding, which is apparently required for the yeast ferrochelatase.

The last step in the biosynthesis of heme is the insertion of ferrous iron into the protoporphyrin IX macrocycle. This reaction is catalyzed by ferrochelatase (protoheme ferrolyase, EC 4.99.1.1) (*1*, *2*), a eukaryotic enzyme located in the matrix side of the inner mitochondrial membrane (*3*, *4*). Ferrochelatase genes and cDNAs have been obtained and sequenced from many sources, such as bacteria (*5*−*7*), yeast (*8*), plants (*9*), frog (*10*), mouse (*11*, *12*), bovine (*13*), and human (*14*). With the development of heterologous overexpression systems, site-directed variants of ferrochelatase can be engineered and overproduced for investigation of the role of specific amino acids in the ferrochelatase reaction mechanism.

The X-ray crystal structure of the *Bacillus subtilis* enzyme has been solved to 1.9 Å resolution (*15*). The structure shows a cleft in a region containing several conserved amino acid residues proposed to be at the active site. Among these residues are a histidine (H183 in *B. subtilis* ferrochelatase and H207 in the murine mature enzyme) and a glutamate (E264 in *B. subtilis* ferrochelatase and E287 in the murine mature enzyme). The active site histidine and glutamate have been advocated to be involved in binding of the metal substrate (*16, 17*) and in catalysis (*18*), respectively. Biophysical characterization of human and mouse ferrochelatase has shown that these enzymes contain a [2Fe−2S] cluster (*19*, *20*). In contrast, the bacterial, yeast, and plant ferrochelatases have no known metal cofactors (*1*).

The proposed catalytic mechanism of ferrochelatase involves the out-of-plane distortion of the free-base proto-

---

[†] This work was supported by the American Cancer Society (Grant BE-248) and the National Institutes of Health (Grant DK51186) (to G. C. F.). Sandia is a multiprogram laboratory operated by Sandia Corporation, a Lockheed Martin Company, for the United States Department of Energy under Contract DE-AC04-94AL85000 (J. A. S.).

* To whom correspondence should be addressed: Prof. John A. Shelnutt, Sandia National Laboratories, Albuquerque, NM 87185-1349. Telephone: 505-272-7160. Fax: 505-272-7077. E-mail: jasheln@unm.edu.

[‡] University of South Florida.

[§] Present address: Departamento de Química, Faculdade de Ciências e Tecnologia, Universidade Nova de Lisboa, 2825 Monte de Caparica, Portugal.

[||] University of New Mexico.

10.1021/bi991346t CCC: $19.00

porphyrin when bound to the active site cleft. This deformation is one that exposes the pyrrole nitrogens to the metal atom promoting the insertion reaction. Evidence for this structural mechanism comes primarily from the strong inhibition of ferrochelatase by N-alkyl porphyrins, which exhibit such a nonplanar distortion (*21*). Indeed, *N*-methylporphyrins have been advocated to be transition state analogues for porphyrin metalation (*22*). Moreover, an antibody raised against a distorted porphyrin, *N*-methyl mesoporphyrin,[1] catalyzed metal insertion into the porphyrin ring (*22, 23*), reinforcing the proposal that distortion of the porphyrin ring is one of the steps of the ferrochelatase catalytic mechanism. Recently, Blackwood et al. (*24*) reported that the catalytic antibody had a different mode of porphyrin binding than that of yeast ferrochelatase. In contrast to the catalytic antibody, the yeast ferrochelatase, an enzyme devoid of a [2Fe−2S] cluster, strained the porphyrin ring conformation with a tilting of all four pyrrole rings in the same direction ("doming"). However, this "doming" distortion could only be detected upon the binding of $Hg^{2+}$ (*24*), which has been reported to be a potent inhibitor of ferrochelatase activity (*4, 21*).

In this study, we have used resonance Raman spectroscopy and other spectroscopic and biochemical techniques to investigate the mode of porphyrin interaction with murine wild-type ferrochelatase and two site-directed mutants. Resonance Raman and UV−vis absorption spectra indicate a nonplanar distortion of the porphyrin macrocycle for various metal and free-base porphyrins bound to the wild-type and engineered variants of murine ferrochelatase. Moreover, the degree of the nonplanar ring distortion is dependent on the mutations introduced in the active site of the enzyme and the type of porphyrin bound. The resonance Raman spectroscopic results on the nonplanar distortion of the murine ferrochelatase-bound porphyrin expand on those previously reported on the mode of interaction between free-base porphyrin and yeast ferrochelatase. For the yeast protein, the enzyme-bound porphyrin displayed significant macrocycle distortion only when $Hg^{2+}$ was also bound to the enzyme. In addition, molecular mechanics calculations of nickel protoporphyrin bound to the active site cleft of the *B. subtilis* ferrochelatase give porphyrin distortions of a magnitude consistent with deformations estimated from shifts in the Raman lines and further elucidate the proposed mechanism.

## MATERIALS AND METHODS

*Materials.* Oligonucleotide primers were synthesized by Cybersyn, Inc., Lenni, PA, and GIBCO BRL. The Chameleon double-stranded, site-directed mutagenesis kit was a product from Stratagene. Sequenase and sequencing kits were from U. S. Biochemical Corp.; [α-$^{35}$S]-dATP was from Dupont/NEN Research Products. Acrylamide and gel reagents were purchased from BioRad. The bicinchoninic acid protein assay reagents were obtained from Pierce Chemical Co. Ni−NTA agarose and the QIAquick PCR purification kit were purchased from QIAGEN. All of the porphyrins used in these studies were from Porphyrin Products (Logan, UT). All other chemicals were of the highest purity available.

*Construction of His-tagged H207N Ferrochelatase Plasmid.* Plasmid pAP1, which contains the murine H207N ferrochelatase mutant cDNA sequence under the control of the alkaline phosphatase promoter, was constructed as previously used for plasmid pAP4 encoding the E287Q mutant (Franco, R. et al., unpublished results). The mutagenic oligonucleotide for H207N was 5′-CTG TTT TCT GCC *A*AC TCC CTG CCG-3′ (mutagenized base is in italics). Clones obtained after the mutagenesis procedure were screened using DNA sequencing according to the dideoxynucleotide chain termination method (*25*). The resulting expression plasmid containing the mutation E287Q was named pAP4. To construct pGF57, an expression plasmid encoding the histidine-tagged H207N ferrochelatase mutant, pAP1, was digested with *Bsp*120 I and *Bam*H I, and the H207N mutation-containing DNA fragment was ligated into pGF47 (Franco, R. et al., unpublished results) previously treated with *Bsp*120 I and *Bam*H I.

*Enzyme Preparation.* Recombinant murine liver ferrochelatase was isolated and purified from hyperproducing DH5α *Escherichia coli* cells containing the ferrochelatase expression plasmid pGF47. The mutant forms of ferrochelatase (E287Q and H207N) were isolated from hyperproducing DH5α *E. coli* cells harboring the corresponding mutated ferrochelatase expression plasmids. The purification scheme for the overproduced wild-type and mutant ferrochelatases will be described elsewhere (Franco, R. et al., unpublished results). The purified, concentrated proteins (typically 200 $\mu$M) in buffer H (20 mM Tris-HCl, pH 8, 10% glycerol, and 0.5 M NaCl) were frozen and stored in liquid nitrogen until use.

*Porphyrin Solutions.* Porphyrin solutions were prepared by dissolving the appropriate amount of powder reagent in 0.1 N KOH (final pH = 13). Stock porphyrin solutions for preparing the Raman and UV−vis absorption samples were typically about 2 mM.

*Raman Samples.* Raman samples were prepared in buffer H. The appropriate volumes of the respective stocks of porphyrin and ferrochelatase were added for a final volume of 500 $\mu$L and a porphyrin concentration of approximately 70 $\mu$M. The samples, contained in a stoppered 3 × 3 mm cross-section optical cell (NSG Precision Cells), were incubated for 30 min under a nitrogen flow in order to lower the oxygen concentration.

Resonance Raman spectra were obtained using the 406.7 nm line of an INNOVA $Kr^+$ laser (Coherent). The spectrometer was a 0.75 m monochromator (Instruments, SA) with a 512 × 2048 pixel $LN_2$-cooled CCD detector. The slit width of 100 $\mu$m for the 2400 groove/mm holographic grating gives a spectral resolution of 2 $cm^{-1}$. The CCD array was cooled by $LN_2$ to 138 K in a 2.8 L dewer and controlled by the CCD3000 controller unit (Instruments, SA). The columns of the CCD chip (EEV) were binned to give 2048 13.5 $\mu$m channels or 0.3 $cm^{-1}$ per channel. The chip is back-illuminated and has visible−NIR antireflection coatings. The spectrometer was interfaced to a 400 MHz Pentium II-based personal computer via an IEEE 488.2 PCI-GPIB interface card (National Instruments), and SpectraMax for Windows software (Instruments, SA) was used to collect the data from the CCD and to control the spectrometer. Position mode was used for CCD detection covering about 500 $cm^{-1}$ of the Raman spectrum. The spectra typically were obtained at room temperature in 3−10 min using 10−20 mW of laser power. Spectra were output as even-X ASCII files for plotting with SigmaPlot (SPSS).

---

[1] Abbreviations: mesoporphyrin, MesoP; protoporphyrin IX, ProtoP; charge-coupled device, CCD; planar, n; nonplanar, np; cetyltrimethylammonium bromide, CTAB; ruffled, *ruf*; saddled, *sad*.

Lorentzian decompositions of the spectra employed the program PeakFit (SPSS). All parameters (center, height, area) were allowed to vary for these Lorentzian area peaks. Peaks were placed only where indicated in the spectra or where clear asymmetry or broadening of lines indicated. The latter case often applied to the structure-sensitive lines $\nu_{10}$ and $\nu_3$, and occasionally $\nu_4$. Curve-fitting was mainly performed to get accurate frequencies for the centers of the lines or to locate the sublines of the structure-sensitive lines. In some regions complicated by spectral crowding of lines, single peaks were used to fit the spectra, even though more peaks were clearly indicated. This was justified, since the frequencies of these lines were not crucial to the interpretation of the Raman data.

*UV−vis Absorption Spectral Titrations.* The titrations of the UV−vis absorption spectra were performed by adding increasing amounts of the respective porphyrin solution made in 0.1 N KOH to 10 $\mu$M protein in buffer H. The final volume of porphyrin solution added was always less than 5% of the total volume, and the pH of the reaction mixture was maintained at 8.0. UV−vis absorption spectra were recorded on a HP9852A diode array spectrophotometer. Acquired spectra were exported as ASCII files and imported into the graphing program SigmaPlot for presentation. The spectra were used to obtain equilibrium dissociation constants ($K_D$) by fitting the absorbance data (Abs), corresponding to the ferrochelatase-bound porphyrin, to the equation

$$Abs = Abs_{\max}[\mathrm{P}]/(K_\mathrm{D} + [\mathrm{P}])$$

where $Abs_{\max}$ represents the theoretical maximal absorbance and [P] the porphyrin concentration. The nonlinear regression analysis program EnzFitter was used to perform the fitting.

*Ferrochelatase Activity Determinations.* Enzymatic activity was determined using a modification of the continuous spectrofluorimetric assay (*26*). Briefly, ferrochelatase activity was monitored by following the rate of consumption of the free-base mesoporphyrin IX [$H_2$(MesoP)] substrate. Kinetic measurements were conducted using a model RSM-1000F spectrofluorometer equipped with a temperature-controlled cell-holder and magnetic stirrer (OLIS, Inc.). The maximum excitation and emission wavelengths for mesoporphyrin IX under the assay conditions were 410 and 620 nm, respectively. The final concentrations of the substrates and enzyme in the reaction mixture were 2 $\mu$M for mesoporphyrin, 2 $\mu$M for $Ni^{2+}$ or $Zn^{2+}$, and 30 nM for ferrochelatase. The reaction was initiated with addition of the metal substrate and was performed at 30 °C.

*Molecular Mechanics Calculations.* The influence of the active site of *B. subtilis* ferrochelatase on the shape of the macrocycle of nickel protoporphyrin IX was investigated using a modified (*27*) DREIDING II (*28*) force-field containing atom types specific for Ni porphyrins and a modified version of Polygraf software (MSI). The force-field has been developed and refined over the past decade and most recently described by Song et al. (*27*) and validated for many Ni-porphyrin systems (*29−36*). The calculations were done by docking Ni(ProtoP) in the ferrochelatase cleft and then minimizing the Ni porphyrin with the atoms of the protein held fixed. Water molecules in the active site were also allowed to move in the minimizations. Since the exact location and orientation of the porphyrin in the binding site is currently unknown, several orientations and locations of Ni(ProtoP) were assumed as initial structures for determining the variability of the macrocyclic structure imposed by the protein. Structures were energy optimized to a force of 0.001 kcal $mol^{-1}$ $Å^{-1}$ without allowing the partial charges on the porphyrin or protein to change during minimization, and an *r*-dependent dielectric constant of 79 was used. Atomic charges for the isolated Ni-protoporphyrin molecule were obtained by using the charge equilibration method (*37*) during energy optimization. For the protein atoms, charges were those used in CHARMM where the hydrogen charge was incorporated into the heavy atom for atom types with implicit hydrogens. The atom types were assigned to the protein atoms by the DREIDING II conversion file of Polygraf.

*Normal-Coordinate Structural Decomposition (NSD).* Normal-coordinate structural decomposition (*38−40*) was used to characterize the calculated structures of the porphyrin macrocycle. The NSD procedure takes a porphyrin structure and determines the distortion from a reference planar macrocycle in terms of equivalent displacements along the normal coordinates of the reference $D_{4h}$-symmetric macrocycle. In this description of the macrocycle distortion, the largest deformations are generally along the lowest frequency modes, and most structures are adequately described by giving the displacements along only the lowest frequency normal coordinate of each out-of-plane symmetry type. The NSD program determines these optimum displacements (as well as those for all of the other normal coordinates). These six out-of-plane displacements give a simple description of the porphyrin distortion that can be displayed as a bar graph. These normal coordinates approximately correspond to the symmetric out-of-plane deformations commonly seen in X-ray crystal structures of symmetrically substituted porphyrins, i.e., the so-called ruffled, saddled, domed, *x*- and *y*-waved, and propellered structures. The ruffling deformation involves twisting of the pyrrole rings of the porphyrin about the metal−nitrogen bond, whereas saddling and doming involve tilting about an axis perpendicular to the metal−nitrogen bond and in the pyrrole plane. Positive and negative deformations have meaning, because of the asymmetric substitution pattern of protoporphyrin. All of these deformations and additional ones that are sometimes important are illustrated elsewhere (*39−41*).

## RESULTS

The UV−vis absorption spectra and resonance Raman spectra of wild-type and mutant ferrochelatase and the complexes with various free-base and nickel porphyrin derivatives are given in Figures 1 through 5, with the nickel porphyrin spectra shown in Figures 1 and 2. Representative UV−vis absorption spectra given in Figure 3 show the changes occurring upon addition of exogenous free-base porphyrin; similar UV−vis spectra were obtained for the nickel porphyrins as well. Several resonance Raman spectra of protein-free solutions of the porphyrins are also given for comparison. The wavelengths of absorption maxima are listed in Table 1, and frequencies of selected resonance Raman lines are listed in Tables 2 and 3.

Nickel porphyrins serve as sensitive probes of the protein environment at the active site and particularly the out-of-

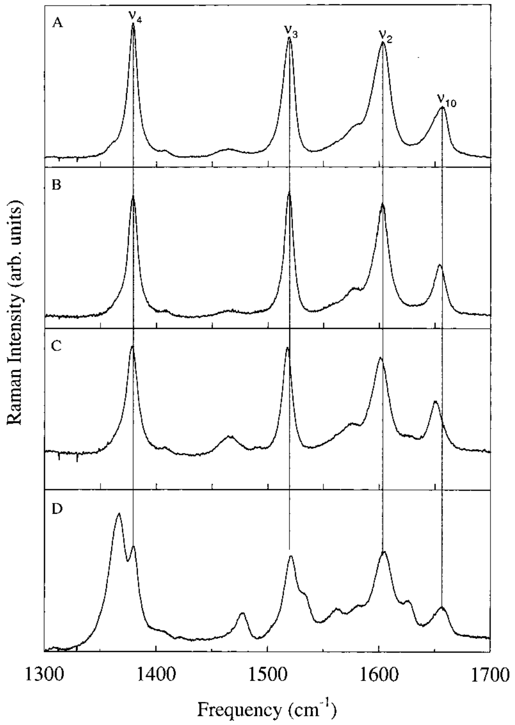

FIGURE 1: Resonance Raman spectra of nickel mesoporphyrin IX [Ni(MesoP)] bound to wild-type and mutant ferrochelatase in pH 8 buffer: (A) Ni(MesoP) in CTAB micellar solution; (B) wild-type ferrochelatase plus 1 equiv of Ni(MesoP); (C) H207N mutant ferrochelatase plus 1 equiv of Ni(MesoP); (D) E287Q mutant plus 1 equiv of Ni(MesoP). Light excitation is at 406.7 nm using a $Kr^+$ laser.

plane forces exerted by the protein on the porphyrin macrocycle. This sensitivity results from the enhanced tendency of porphyrins containing small metals, such as low-spin Ni(II), to undergo deformation like ruffling and saddling that shorten the $Ni-N_{pyrrole}$ bond lengths. Thus, a Ni porphyrin is more responsive to the out-of-plane forces exerted by the protein matrix. The functional relevance of the use of nickel porphyrin derivatives in this study was assessed by determining the enzymatic activity with $Ni^{2+}$ and mesoporphyrin IX as substrates in the ferrochelatase-catalyzed reaction. Triplicate determinations of the enzymatic activity indicated a value of about 5% of that obtained with $Zn^{2+}$ and mesoporphyrin as substrates (*26*), suggesting that nickel mesoporphyrin can be a product of the metalation reaction catalyzed by ferrochelatase.

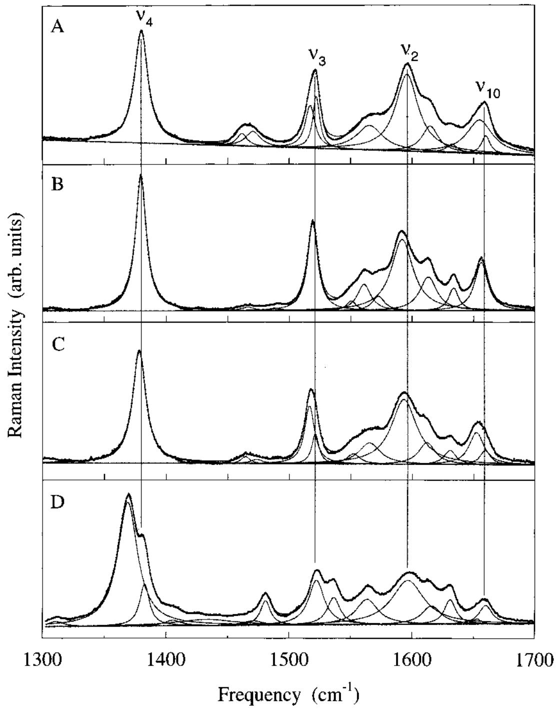

FIGURE 2: Resonance Raman spectra of nickel protoporphyrin IX [Ni(ProtoP)] bound to wild-type and mutant ferrochelatase in pH 8 buffer: (A) Ni(ProtoP) in buffered solution; (B) wild-type ferrochelatase plus 1 equiv of Ni(ProtoP); (C) H207N mutant ferrochelatase plus 1 equiv of Ni(ProtoP); (D) E287Q mutant plus 1 equiv Ni(ProtoP). Light excitation is at 406.7 nm using a $Kr^+$ laser. The gray curves indicate the individual peaks determined from Lorentzian decomposition of the spectra and their sum. The dotted line indicates the linear background determined in the curve fitting. Some of the peak positions, widths, and area ratios are given in Table 3.

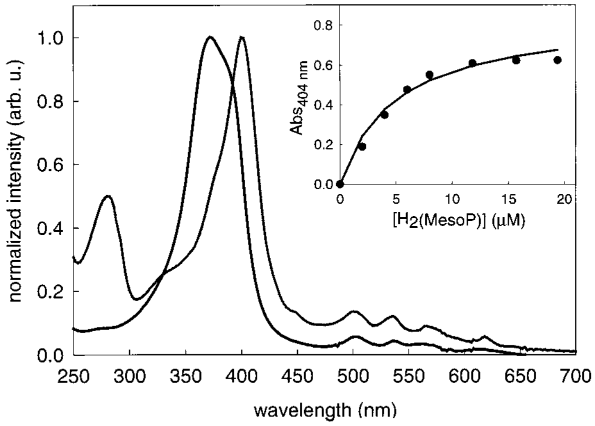

FIGURE 3: UV–vis absorption spectrum of free-base mesoporphyrin IX [$H_2$(MesoP)] in solution (solid) and bound to wild-type ferrochelatase (FC) with $H_2$(MesoP)/FC (molar ratio) = 1 (gray). The inset represents the titration of ferrochelatase with $H_2$(MesoP) (filled circles). Changes in absorbance at 404 nm were plotted as function of [$H_2$(MesoP)] and fitted to an hyperbolic equation (solid line) for determination of the dissociation constant (see Material and Methods for details). The determined $K_D$ was 5.0 $\mu$M.

*Ni(MesoP)–Ferrochelatase Complexes.* UV–vis absorption spectral changes observed upon adding nickel mesoporphyrin [Ni(MesoP)] to wild-type ferrochelatase indicate binding of the porphyrin to the protein. Ni(MesoP) in solution at pH 8 shows a broad and blue-shifted Soret band. In contrast, upon addition of 1 equiv of Ni(MesoP) to a ferrochelatase solution at pH 8, the Soret band red-shifts and narrows, probably indicating a monomeric species (Table 1). Furthermore, the spectra obtained upon the addition of extra equivalents (up to 5) of nickel mesoporphyrin were analyzed in order to determine the nature of the ferrochelatase-bound component. The titration data (not shown) and 1:1 binding analysis were similar to those for the $H_2$(MesoP)–ferrochelatase complex shown in Figure 3 (see below). The equilibrium dissociation constant $K_D$ obtained from fitting the titration data for Ni(MesoP) was 4.3 $\mu$M, almost the same as for $H_2$(MesoP), and thus $K_D$ is consistent with strong binding at a single site.

The resonance Raman spectra of ferrochelatase with nickel mesoporphyrin [Ni(MesoP)] bound are shown in Figure 1 along with monomeric Ni(MesoP) in CTAB solution for comparison. The frequencies obtained from Lorentzian

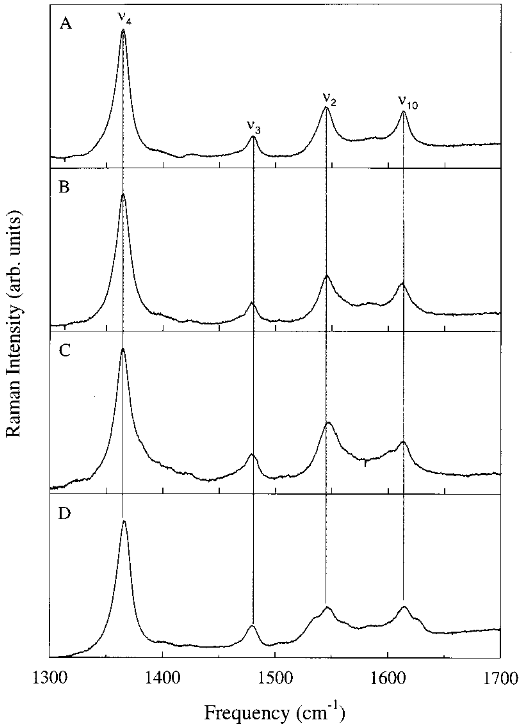

FIGURE 4: Resonance Raman spectra of free-base mesoporphyrin IX [$H_2$(MesoP)] bound to wild-type and mutant ferrochelatase: (A) $H_2$(MesoP) in pH 8 buffered CTAB solution; (B) wild-type ferrochelatase plus 1 equiv of $H_2$(MesoP) at pH 8; (C) H207N mutant with 1 equiv of $H_2$(MesoP) at pH 8; (D) E287Q mutant with 1 equiv of $H_2$(MesoP) at pH 8.0. Light excitation is at 406.7 nm using a Kr$^+$ laser.

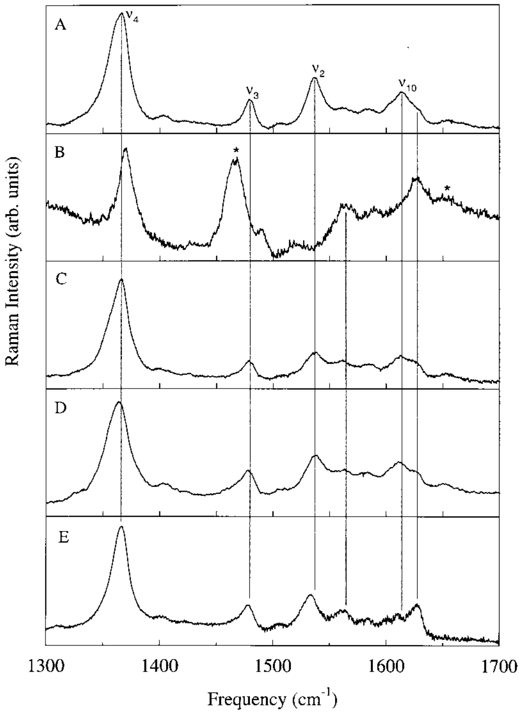

FIGURE 5: Resonance Raman spectra of free-base protoporphyrin IX [$H_2$(ProtoP)] bound to wild-type and mutant ferrochelatase in pH 8 buffer: (A) $H_2$(ProtoP) in buffered CTAB solution; (B) wild-type ferrochelatase without added protoporphyrin; (C) wild-type ferrochelatase plus 1 equiv of $H_2$(ProtoP); (D) H207N ferrochelatase plus 1 equiv of $H_2$(ProtoP); (E) E287Q mutant without added protoporphyrin. Light excitation is at 406.7 nm using a Kr$^+$ laser. Asterisk indicates lines of aqueous buffer H.

Table 1: Shifts in Porphyrin Soret Bands upon Binding to Wild-type and Mutant Ferrochelatase

| porphyrin[a] | protein | free porphyrin, Soret band (nm) | protein-bound porphyrin,[b] Soret band (nm) | Soret band shift (nm) |
|---|---|---|---|---|
| $H_2$(MesoP) | wild-type | 372 | 404 | 32 |
| Ni(MesoP) | wild-type | 380 | 394 | 14 |
| $H_2$(ProtoP)* | wild-type | 400 | 413 | 13 |
| Ni(ProtoP) | wild-type | 382 | 386 | 4 |
| Ni(ProtoP) | H207N | 382 | 384 | 2 |
| Ni(ProtoP) | E287Q | 382 | 390 | 8 |

[a] Porphyrin stock solutions were made in 0.1 M KOH, pH = 13, except for that of $H_2$(ProtoP), which is denoted with an asterisk. The $H_2$(ProtoP) was made in water containing 0.4% Triton X-100 and 4 mM $NH_4OH$. Porphyrins were diluted in buffer H or in buffer H containing 10 $\mu$M protein to a final concentration of 10 $\mu$M and pH ~ 8.2. [b] Porphyrins were added to ferrochelatase (wild-type or mutants) in buffer H at a molar ratio of 1:1.

decomposition of the Raman spectra are listed in Table 2. In general, the Raman spectrum Ni(MesoP) in CTAB micelles at pH 8 (Figure 1A) is almost identical to the spectra of other nickel porphyrins such as nickel protoporphyrin IX [Ni(ProtoP)] (*42*), uroporphyrin [Ni(UroP)] (*42*), and octaethylporphyrin [Ni(OEP)] (*43*). All of these nickel porphyrins in solution exhibit an equilibrium mixture of planar and ruffled conformers, generally with somewhat higher populations of the nonplanar conformer based on the area intensities of the two sublines making up the line shape of $\nu_{10}$. The relative concentrations of these conformers are only slightly influenced by aggregation and solvation effects (*42*). The coexistence of planar and nonplanar forms leads to broadening and asymmetry of the structure-sensitive Raman lines.

Binding of Ni(MesoP) to wild-type ferrochelatase is indicated in the resonance Raman spectrum shown in Figure 1B by the remarkable narrowing of the structure-sensitive Raman lines including $\nu_3$, $\nu_2$, and $\nu_{10}$. The narrowing for ferrochelatase is particularly evident in $\nu_{10}$, which decreases from approximately 20 cm$^{-1}$ for Ni(MesoP) in buffered CTAB solution to 12.6 cm$^{-1}$ in the protein-bound form. The $\nu_{10}$ line typically shows the largest downshifts upon ruffling of the macrocycle, which brings about the broadest line width for the solution mixture of planar and ruffled Ni(MesoP) species. Another indication of the binding to ferrochelatase is the downshifts in the peak frequencies of all of the structure-sensitive lines. For the Ni(MesoP)−ferrochelatase complex, the downshifts become larger as the marker-line frequencies increase. This is the typical pattern of downshifts in the structure-sensitive lines when ruffling is the cause (*42*−*44*). For example, the downshifts of the nonplanar form for the CTAB solution are 4.9, 7.1, and 7.8 cm$^{-1}$ for $\nu_3$, $\nu_2$, and $\nu_{10}$, respectively.

For protein-bound Ni(MesoP), both the narrowings and downshifts are a consequence of the disappearance of the mixture of conformers occurring upon formation of a homogeneous ferrochelatase-bound conformer. This bound Ni(MesoP) species is more ruffled than the nearly planar conformer found in the solution studies, but not as ruffled as the solution-ruffled conformer based on the size of the downshifts. From Lorentzian decomposition of the spectra in Figure 1, Ni(MesoP) in solution has $\nu_{10}$ at 1657.5 cm$^{-1}$ for the planar conformer and at 1649.7 cm$^{-1}$ for the ruffled conformer, a downshift of 7.8 cm$^{-1}$ for the nonplanar

Table 2: Frequencies (cm$^{-1}$) of Some of the Raman Lines in the 1300−1700 cm$^{-1}$ Region Obtained from Lorentzian Decomposition of the Spectra of Ferrochelatase and the H207N and E287Q Mutants with and without Bound Ni(MesoP), Ni(ProtoP), $H_2$(ProtoP), and $H_2$(MesoP)

| | $\nu_4$ | $\nu_3$, np | $\nu_3$, p | $\nu_2$, np | $\nu_2$, p | $\nu_a$[a] | $\nu_b$[a] | $\nu_{10}$, np | $\nu_{10}$, p | $\nu_{vinyl}$ |
|---|---|---|---|---|---|---|---|---|---|---|
| | | | | Ni(MesoP) | | | | | | |
| CTAB | 1378.7 | 1515.9 | 1520.8 | 1597.9 | 1605.0 | | | 1649.7 | 1657.5 | |
| FC | 1378.7 | 1518.6[b] | | 1603.0[b] | | | | 1653.8[b] | | |
| H207N | 1377.9 | 1517.3 | | 1595.4 | 1602.2 | | | 1650.8 | | |
| | | | | | | 1560.6[c] | | | | 1627.5 |
| E287Q | 1380.3 | 1520.4 | | 1604.0 | | | | **1653.4**[d] | 1659.4 | |
| | 1365.4[c] | 1476.9 | | 1534.0 | | 1561.3 | 1580.0 | | | 1626.6 |
| | | | | Ni(ProtoP) | | | | | | |
| CTAB | 1380.0 | 1517.2 | 1522.2 | 1595.9 | | | | **1654.9** | 1660.3 | 1632.6 |
| FC | 1379.6 | 1519.1 | | 1591.9 | | | | 1656.1 | | 1633.7 |
| H207N | 1378.2 | **1516.5** | 1521.2 | 1593.3 | | | | **1652.0** | 1659.1 | 1630.8 |
| E287Q | 1382.5 | 1522.2 | | 1596.7 | | | | 1652.6 | **1659.6** | 1630.9 |
| | 1369.0[c] | 1480.8 | | 1536.2 | | 1563.4 | 1597.6 | 1615.8 | | |
| | | | | $H_2$(MesoP) | | | | | | |
| CTAB | 1356.9 **1364.0** | 1479.7 | | 1544.3 | | 1566.7 | 1587.8 | 1613.2 | | |
| FC | 1364.5 | 1478.9 | | 1544.9 | | 1557.1 | 1582.5 | 1612.1 | | |
| H207N | 1364.4 | 1479.3 | | 1546.5 | | 1563.0 | ∼1590 | 1613.6 | | |
| E287Q | 1362.0 | 1478.8 | | 1546.5 | | 1561.4 | 1586.4 | 1614.0 | | |
| | 1366.6[c] | | | 1533.5 | | | | | | 1627.2 |
| | | | | $H_2$(ProtoP) | | | | | | |
| CTAB | 1360.0 1368.1 | 1478.9 | | 1536.7 | | 1561.6 | 1584.1 | 1614.3 | | 1626.3 |
| FC | 1356.4 **1366.6** | 1477.9 | | 1530.4 | 1537.8 | 1560.7 | 1584.6 | 1613.6 | | 1626.0 |
| H207N | 1355.5 **1365.0** | 1478.2 | | 1536.8 | | 1561.7 | 1583.1 | 1612.0 | | 1626.8 |
| | | | | FC | | | | | | |
| | 1370.3 | | | 1563.3 | | 1588.9 | 1608.6 | 1626.5 | | 1626.5 |
| | | | | H207N | | | | | | |
| | 1368.3 | | | | | ∼1570 | | ∼1629 | | |
| | | | | E287Q | | | | | | |
| | 1365.4 | 1478.1 | | 1532.5 | | 1561.8 | 1583.8 | 1610.9 | | 1627.0 |

[a] Raman lines that have not been assigned. [b] These frequencies are that of a single line representing both sublines in the Lorentzian decompositons. [c] Lines assigned to endogenous porphyrin. [d] The frequency is in bold type for the subline that overwhelmingly dominates.

Table 3: Spectral Decomposition of $\nu_{10}$ of Nickel Protoporphyrin Bound to Ferrochelatase, the H207N Mutant, and Free in Solution

| Raman line | frequency (cm$^{-1}$) | width (cm$^{-1}$) | area ratio, np/p |
|---|---|---|---|
| | buffer H | | |
| $\nu_{10}$, nonplanar | 1654.9 ± 0.4 | 22.9 ± 0.6 | 5.3 |
| $\nu_{10}$, planar | 1660.3 ± 0.2 | 8.1 ± 0.8 | |
| | 1:1 FC | | |
| $\nu_{10}$, nonplanar | 1656.1 ± 0.1 | 12.8 ± 0.1 | >10 |
| | 1:1 H207N | | |
| $\nu_{10}$, nonplanar | 1652.0 ± 0.4 | 14.3 ± 0.7 | 2.6 |
| $\nu_{10}$, planar | 1659.1 ± 0.4 | 10.8 ± 1.1 | |

conformer (Table 2). For comparison, this downshift is smaller than the approximately 20 cm$^{-1}$ downshift observed for the ruffled crystal structure of Ni(OEP) compared with the planar crystalline forms (*45*). The ruffling angle between the planes of the pyrrole rings of the ruffled Ni(OEP) crystalline form is 32.8° (*46*, *47*). The frequency of $\nu_{10}$ of the unique conformer of Ni(MesoP) bound to ferrochelatase is located at 1653.8 cm$^{-1}$, a downshift from the planar species frequency of only 3.7 cm$^{-1}$. This shift indicates a significant degree of ruffling, while the narrowness of the line is consistent with a single homogeneous binding site. It is important to remember that the relationship between the Raman frequency and the ruffling deformation is nonlinear (vide infra), with the dependence (slope) increasing as the ruffling increases. Thus, the change in ruffling may be significant even for small downshifts in the structural marker lines when the magnitude of ruffling is in the range from 0 to 2 Å (see Figure 8).

Binding of Ni(MesoP) to the H207N mutant results in a similar but larger change in the resonance Raman spectrum as shown in Figure 1C. A narrowing of the structure-sensitive lines is observed for the mutant, although the narrowing is not so dramatic as for the wild-type. On the other hand, the decrease in frequencies of the structure-sensitive lines is greater for the mutant. For example, $\nu_{10}$ downshifts to 1650.8 cm$^{-1}$, a decrease of 6.7 cm$^{-1}$ from the near planar form of Ni(MesoP) in buffered CTAB solution. As for the wild-type, the downshifts for the lines increase with the frequency of the particular Raman line and thus indicate substantial ruffling of the macrocycle.

A new weak line appears at 1628 cm$^{-1}$ for the H207N mutant with added Ni(MesoP). This vinyl mode is also present in the spectrum of H207N without added porphyrin, indicating a small amount of endogenous free-base protoporphyrin [$H_2$(ProtoP)] that remains bound during isolation of the protein (see Table 2).

For the E287Q mutant, there is scant evidence of binding of Ni(MesoP) to the protein. Indeed, binding of an entire equivalent of Ni(MesoP) is not expected, because about 15% of the binding sites are already occupied by $H_2$(ProtoP), which is strongly bound to the mutant ferrochelatase as isolated (Franco, R. et al., unpublished results). The structure-sensitive line frequencies assigned to Ni(MesoP) are clearly evident, superimposed on the spectrum of endogenous $H_2$(ProtoP), in the Raman spectrum shown in Figure 1D. These lines are not significantly shifted or narrowed from the CTAB solution values. Specifically, $\nu_{10}$ is as broad, and the sublines

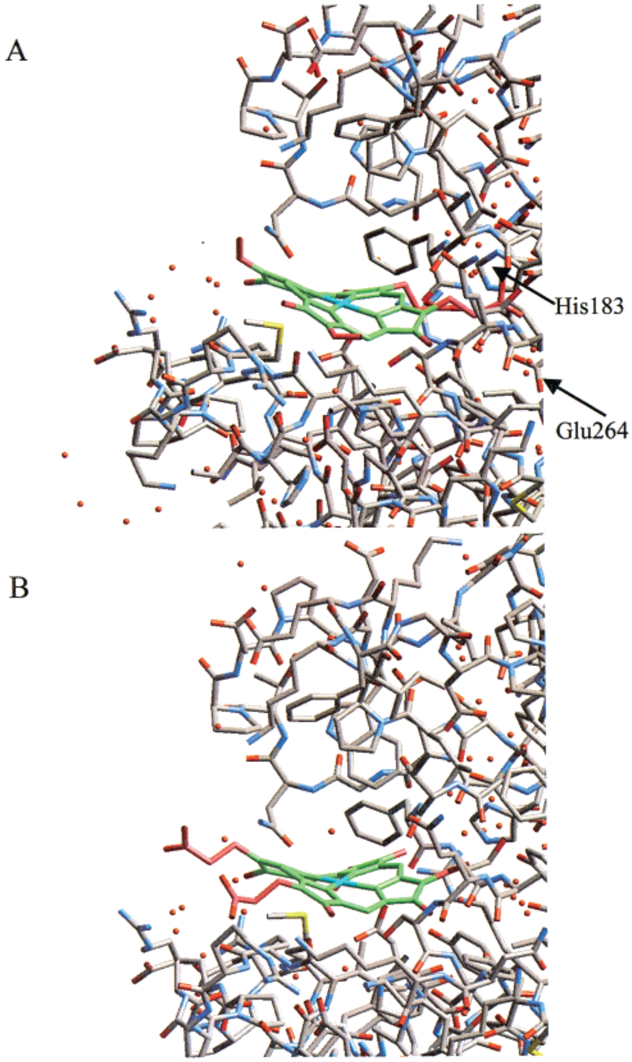

FIGURE 6: The active site of *B. subtilis* ferrochelatase showing the conformation of energy minimized Ni(ProtoP) (and water molecules, not shown) for two low-energy structures: (A) propionates directed into the protein, 44.7 kcal/mol; (B) propionates directed toward the exterior of the protein, 49.4 kcal/mol.

have nearly the same frequency as in the pH 8 CTAB solution. However, spectral decomposition reveals that the intensity of the subline of the ruffled (np) species at 1653.4 $cm^{-1}$, near the frequency for wild-type ferrochelatase, is much larger than for the planar (p) subline at 1659.4 $cm^{-1}$ (area ratio, np/p = 3.2). For Ni(MesoP) in solution, the intensities are more nearly equal (np/p = 1.7). This suggests that a fraction of the added 1 equiv of Ni(MesoP) binds to the protein.

The lines of endogenous $H_2$(ProtoP) in the spectrum of the E287Q mutant in the presence of 1:1 Ni(MesoP)/protein (Figure 1E) also demonstrate that endogenous $H_2$(ProtoP) is not displaced by Ni(MesoP). The spectrum of endogenous $H_2$(ProtoP) of E287Q mutant (shown in Figure 5E) is different from the CTAB solution spectrum of $H_2$(ProtoP) (Figure 5A), especially in the relative intensities of the lines. The Raman spectrum of protein-bound $H_2$(ProtoP) does not change when Ni(MesoP) is added. This is most easily seen in the resolved vinyl mode at 1626.6 $cm^{-1}$. The vinyl mode is only a shoulder on $\nu_{10}$ in the $H_2$(ProtoP) solution spectrum.

*Ni(ProtoP)−Ferrochelatase Complexes.* UV−vis absorption spectral changes, observed upon adding Ni(ProtoP) to wild-type ferrochelatase, indicate specific binding of the porphyrin to the protein. Ni(ProtoP) in solution at pH 8 shows a broad and blue-shifted Soret band. Upon addition of 1 equiv of Ni(ProtoP) to a ferrochelatase solution at pH 8, the Soret band red-shifts and narrows, indicating a monomeric bound species (Table 1). The dissociation constant for the ferrochelatase−Ni(ProtoP) complex was determined from the fitting of the data obtained upon addition of extra equivalents (up to 5) of nickel protoporphyrin to ferrochelatase. The results (data not shown) are similar to those for the $H_2$(MesoP)−ferrochelatase complex (Figure 3), indicating a strongly bound 1:1 complex. The observed red-shifts of the Soret absorbance maxima of nickel protoporphyrin upon binding of site-directed ferrochelatase variants are also indicated in Table 1.

The complex between ferrochelatase and Ni(ProtoP) is similar to the complex with Ni(MesoP) based on the resonance Raman data. The resonance Raman spectrum of Ni(ProtoP) in aqueous solution at pH 8 is shown in Figure 2A for the region of the structure-sensitive lines for comparison with Ni(ProtoP) bound to ferrochelatase. Just as for Ni(MesoP), formation of the 1:1 complex between Ni(ProtoP) and wild-type ferrochelatase (Figure 2B) results in a narrowing of the lines. Specifically, for $\nu_{10}$, the line narrows from 20 $cm^{-1}$ in solution to 12.8 $cm^{-1}$ (Table 3), because the solution mixture of planar and nonplanar forms disappears for the ferrochelatase complex. Further, the frequencies of the structure-sensitive lines also decrease, indicating that the planar and nonplanar solution forms coalesce to a homogeneous conformation of moderate nonplanarity. The downshifts from planar Ni(ProtoP) at pH 8 (1660.3 $cm^{-1}$) are 0.4, 3.1, 4.0, and 4.2 $cm^{-1}$ for $\nu_4$, $\nu_3$, $\nu_2$, and $\nu_{10}$, respectively. The downshifts relative to the planar form of Ni(ProtoP) in aqueous solution at pH 13 in the absence of CTAB are similar. The downshifts show the monotonic decrease with the decreasing frequencies of the Raman marker lines expected for ruffling. Thus, the spectral changes upon binding of Ni(ProtoP) to ferrochelatase are entirely consistent with those observed for Ni(MesoP) binding.

The vinyl substituents appear to be influenced by binding to ferrochelatase as well, since the vinyl stretching mode near 1633 $cm^{-1}$ is much stronger in the spectrum of Ni(ProtoP)−ferrochelatase complex than in the solution spectra. The apparent increase in intensity of the vinyl mode partly results from the line narrowing associated with the homogeneous macrocycle conformation, but the particular vinyl orientations dictated by the active site in the protein is probably important as well. Specifically, curve fitting gives the vinyl-mode line width for Ni(ProtoP) bound to ferrochelatase at 9.8 $cm^{-1}$, compared with 12.6 $cm^{-1}$ in buffer and 12.2 and 11.2 $cm^{-1}$ for the H207N and E287Q mutants, respectively. Clearly, the binding site of the wild-type protein is more homogeneous with respect to the vinyl group interactions in the mutant proteins or in solution with or without detergent. However, the narrowing alone does not account for the increase in intensity evident in Figure 2. Thus, the intensification probably results from a specific orientation of the vinyl groups with respect to the macrocycle.

One-to-one binding of Ni(ProtoP) to ferrochelatase, which is evident from the UV−vis absorption data, is further supported by resonance Raman spectra of a solution containing 3 equivs of Ni(ProtoP). These spectra (not shown), which contain mostly unbound Ni(ProtoP), show broader lines with higher frequencies more characteristic of the spectra of Ni(ProtoP) in aqueous solution at pH 8. The vinyl Raman line also weakens as expected if most of the Ni(ProtoP) is unbound.

The one-to-one complex of Ni(ProtoP) with H207N mutant also shows the same spectral changes as the Ni(MesoP) complex. In particular, the Raman spectrum in Figure 2C shows mostly larger downshifts in the structure-sensitive lines, just as did this mutant for the Ni(MesoP) complex. An exception is the vinyl-sensitive $\nu_2$ line. This line actually upshifts relative to the 1:1 wild-type position, while the vinyl mode itself downshifts by 3 $cm^{-1}$. This suggests different vinyl group positions in the mutant, either because of the increased nonplanar distortion or because of a specific localized interaction between the protein and the vinyl groups. The structure-sensitive lines are a bit broader for the mutant than for the wild-type protein, indicating increased heterogeneity in the binding site of the mutant.

The detailed results of the Lorentzian spectral decomposition for Ni(ProtoP) in solution and bound to ferrochelatase and the H207N mutant are given in Table 3 for $\nu_{10}$. Both planar and ruffled sublines are indicated for Ni(ProtoP) in buffer and for the H207N mutant, but only a single homogeneous ruffled form is supported for wild-type ferrochelatase. The degree of ruffling for the ruffled-bound form is about the same as that for the solution-ruffled form based on the frequencies. On the other hand, the heterogeneity in the macrocyclic conformation for the ruffled-bound porphyrin is much less than for the porphyrin in solution based on the decreased line widths.

As for the Ni(MesoP) complexes, there is only weak support for binding of Ni(ProtoP) to the E287Q mutant in the resonance Raman spectrum shown in Figure 2D; $\nu_{10}$ is as broad and has nearly the same frequency as in the pH 8 solution (Figure 2A). However, in this case, the np/p intensity ratio is much less than one (Table 2). The other structure-sensitive lines also have frequencies that are similar to those for Ni(ProtoP) in solution at pH 8, and they are certainly higher than for the wild-type. Just as for Ni(MesoP), the spectrum of the endogenous free-base protoporphyrin bound to the mutant (Figure 5D) is apparently not altered by the addition of 1 equiv of Ni(ProtoP). Thus, the resonance Raman data for the E287Q mutant indicate that neither Ni(ProtoP) nor Ni(MesoP) are able to displace free-base porphyrin bound at the active site. There is some weak evidence to support binding to the unoccupied sites. In particular, spectral decomposition suggests that if the porphyrin is bound, then the interaction with the E287Q protein shifts the equilibrium in favor of a nearly planar species. This conclusion is based on increased frequencies of $\nu_4$, $\nu_3$, and $\nu_2$ and the large relative intensity of the planar subline of $\nu_{10}$ (Table 2).

*$H_2$(MesoP)−Ferrochelatase Complexes*. UV−vis absorption spectral changes that are observed upon adding free-base mesoporphyrin to wild-type ferrochelatase are similar to the changes observed for the Ni porphyrins, and the changes indicate specific binding of the porphyrin to the protein. In particular, $H_2$(MesoP) in solution at pH 8 shows a broad and blue-shifted Soret band (Figure 3, solid line). Upon addition of 1 equiv of $H_2$(MesoP) to a ferrochelatase solution at pH 8, the Soret band red-shifts and narrows, indicating a monomeric protein-bound species (Figure 3, gray line). Further, the nature of the ferrochelatase-bound component was assessed from the analysis of the spectra obtained upon addition of extra equivalents (up to 5) of $H_2$(MesoP) to ferrochelatase. The observed red-shift of the Soret absorbance maximum of $H_2$(MesoP) upon binding of wild-type ferrochelatase is indicated in Table 1 and Figure 3. The Soret absorbance maximum of ferrochelatase-bound $H_2$(MesoP) (404 nm) was determined from the difference in the spectrum of the 1:1 complex of $H_2$(MesoP) and ferrochelatase and the spectra of free protein and free porphyrin at the same concentrations. When these absorbance data were plotted vs the concentration of added $H_2$(MesoP), an hyperbolic type of behavior was obtained (inset of Figure 3). Curve fitting with an expression (see Materials and Methods) that assumes 1:1 binding gave an adequate fit to the data as shown in Figure 3. A $K_D$ value of 5.0 $\mu$M was obtained with a $\chi$-squared mean deviation of $1.4 \times 10^{-3}$. $Abs_{max}$, which corresponds to the maximum value attained by the absorbance at 404 nm, was determined as 0.85 from the fit. Weak nonspecific binding or an alteration of the state of aggregation of the unbound porphyrin may also be indicated by the small systematic errors in the curve fit.

The resonance Raman spectra of free-base mesoporphyrin and the ferrochelatase−$H_2$(MesoP) complexes are shown in Figure 4. Whether compared to $H_2$(MesoP) in buffered CTAB (Figure 4A) or in 0.1 N KOH (not shown), the structure-sensitive lines are slightly shifted for wild-type ferrochelatase with 1 equiv of $H_2$(MesoP) (see Figure 2B and Table 2). Specifically, $\nu_3$ and $\nu_{10}$ are downshifted for wild-type (∼1 $cm^{-1}$) and possibly for the H207N mutant. This result is consistent with that for binding of Ni porphyrins to ferrochelatase. In contrast, the frequency of $\nu_2$ appears to be upshifted slightly. For the E287Q mutant, addition of $H_2$(MesoP) shows little effect on the spectrum upon binding the added porphyrin. In addition, the endogenously bound porphyrin is not displaced, since its Raman lines are still evident in the spectrum (cf. Figure 4D and Figure 5D).

*$H_2$(ProtoP)−Ferrochelatase Complexes.* UV−vis absorption spectral changes observed upon adding free-base protoporphyrin [$H_2$(ProtoP)] to wild-type ferrochelatase indicate binding of the porphyrin to the protein. $H_2$(ProtoP) in solution at pH 8 shows a broad and blue-shifted Soret band. Upon addition of 1 equiv of $H_2$(ProtoP) to a ferrochelatase solution at pH 8, the Soret band red-shifts and narrows, probably indicating a monomeric bound species (Table 1). Adding extra equivalents (up to 5) of $H_2$(ProtoP) gave spectra that were analyzed to determine the equilibrium dissociation constant for the ferrochelatase complex (data not shown). The observed red-shift of the Soret absorbance maxima of $H_2$(ProtoP) upon binding of wild-type ferrochelatase is indicated in Table 1.

In the case of wild-type ferrochelatase, the resonance Raman spectrum of the $H_2$(ProtoP) complex shows that there is a small residual amount of porphyrin bound to the protein as isolated. Figure 5B shows the Raman spectrum of ferrochelatase at pH 8, and a weak porphyrin Raman spectrum is evident. However, this spectrum differs considerably from the spectrum of $H_2$(ProtoP) in CTAB micelles at pH 8 shown in Figure 5A.

Figure 5C also shows the spectrum of the wild-type ferrochelatase with 1 equiv of $H_2$(ProtoP) added. Although the spectrum differs from as-isolated ferrochelatase, it shows some evidence of a significant fraction of a minor species with a spectrum that is similar to that of the residually bound porphyrin species. This is particularly evident in the strength of the shoulder at about 1626 $cm^{-1}$ and possibly the slightly increased intensity near 1560 $cm^{-1}$.

Figure 5D shows the spectrum of the H207N mutant with 1 equiv of $H_2$(ProtoP). The spectrum is very close to that of the wild-type protein with added $H_2$(ProtoP). Two significant differences are that H207N has a different line shape for $\nu_4$ and a weaker vinyl mode than the wild-type protein.

The spectrum of endogenous free base bound to the E287Q mutant in Figure 5E appears to be a mixture of two forms: the spectrum of one species is similar to that of the residual $H_2$(ProtoP) bound to wild-type ferrochelatase and the spectrum of the other species is similar to that of $H_2$(ProtoP) in the CTAB solution. Specifically, intensity from the former species is evident at about 1627 and 1562 $cm^{-1}$ superimposed on a spectrum that is close to that of the free base in CTAB solution (Figure 5A). Apparently, some of the added porphyrin is bound in a manner similar to that which remains bound during ferrochelatase preparation (Figure 5B), while some of the porphyrin is almost unaffected by binding and has a spectrum like that of $H_2$(ProtoP) in the hydrophobic environment of micelles. The protein and micellar environments do differ, however, as can be seen especially in the lower frequency of the line at 1532.5 $cm^{-1}$ for the E287Q mutant and at 1536.7 $cm^{-1}$ for solution $H_2$(ProtoP).

*Molecular Simulations of Ni(ProtoP) Binding to B. subtilis Ferrochelatase*. The resonance Raman data for Ni(ProtoP) bound to murine ferrochelatase can be interpreted in the clearest possible way, since it remains four-coordinate and, unlike free-base porphyrin, it has no pyrrole protons and nitrogen lone pairs that can interact with the protein. Thus, we chose to investigate the structural consequences of binding of Ni(ProtoP) at the active site of the known X-ray structure of the *B. subtilis* protein. It should be noted that these calculations would not reflect any rearrangements of the protein that occur upon substrate binding. Nevertheless, our goal is simply to determine whether the distortion that occurs upon binding is consistent with that indicated by the shifts in the structure-sensitive Raman lines.

Figure 6 shows two representative Ni(ProtoP) structures obtained by energy-optimization within the cleft of the *B. subtilis* X-ray crystal structure, and the normal-coordinate structural decomposition analyses of these and other Ni(ProtoP) structures are illustrated in Figure 7. The two low-energy locations shown have the propionate groups of the heme oriented toward the interior of ferrochelatase (Figure 6A) and toward the exterior solvent (Figure 6B), respectively. Other initial locations of the porphyrin, mostly further into the cleft, give structures that have about the same total distortion (root-squares displacements of the 24 macrocyclic atoms from the mean plane). For these other porphyrin locations and orientations, significant deformations other than ruffling occur. The energies of the complexes vary considerably, but it should be remembered that the protein in these calculations is not allowed to adjust to the presence of the porphyrin (other than the water molecules in the cavity that are allowed to move). All energies are lower than that of the isolated Ni(ProtoP)-ruffled form, except for the two highest energy structures. The energies are lower than the free porphyrin primarily because of favorable van der Waals interactions with the protein.

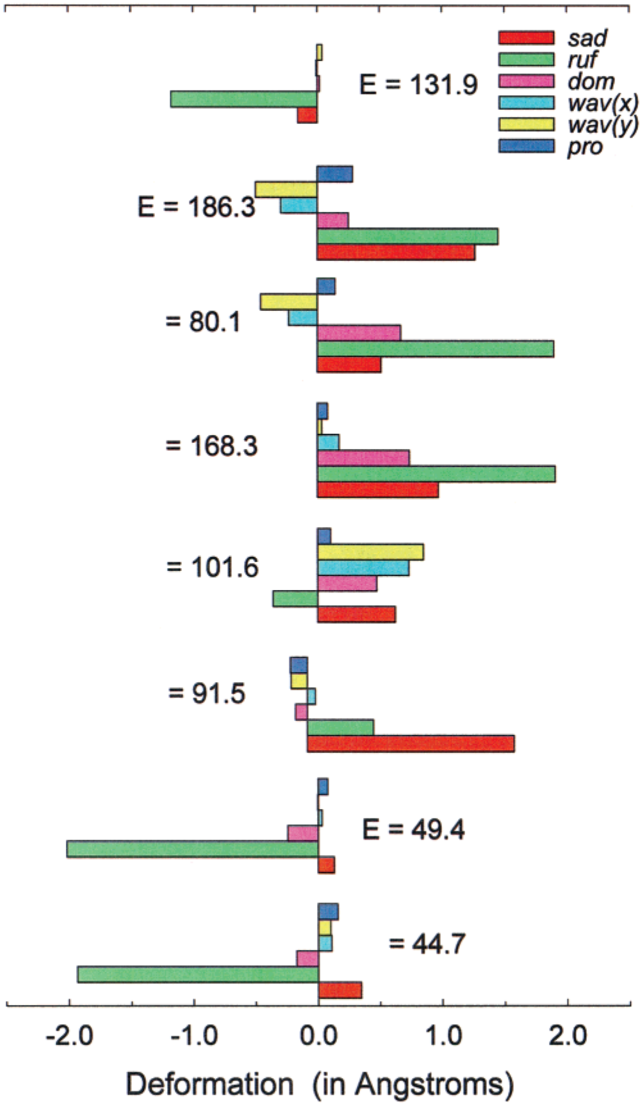

FIGURE 7: NSD deformations of energy-optimized Ni(ProtoP) isolated (top) and located at seven different locations in the cleft of *B. subtilis* ferrochelatase. Water molecules in the cleft were movable in the simulations, but the protein and other water molecules were fixed at the X-ray structure coordinates. The total energies are given for each structure. The lowest energy structure (bottom) has the propionates oriented toward the interior of the protein, but the energy of the next lowest energy structure has the propionates oriented toward the solvent. The high-energy structures are generally located deeper in the crevice.

## DISCUSSION

A postulated role for ferrochelatase during the catalytic reaction is to force the porphyrin ring toward a distorted conformation in which the two pyrrole nitrogen electrons are more accessible to the incoming metal ion substrate (*22*, *24*). One step in understanding the ferrochelatase catalytic mechanism involves the determination of whether a nonplanar porphyrin distortion is caused by ferrochelatase and, if so, the identification of the type of macrocyclic distortion and the protein determinants responsible for the distortion. In the work reported here, we have investigated the mechanism of porphyrin binding to wild-type and site-directed-mutant forms of ferrochelatase and demonstrated that a modest nonplanar distortion of the macrocycle occurs upon binding. Furthermore, the mutations of amino acids proposed to be involved in substrate binding or catalysis do influence the magnitude of the macrocycle distortion, confirming their presence at the active site and possibly their role in catalysis.

One-to-one binding of free-base or nickel porphyrins to ferrochelatase is apparent from the UV−vis absorption and resonance Raman spectra obtained by titration of ferrochelatase with the porphyrins. It is important to note that monomeric porphyrin solutions, at a concentration required for the resonance Raman studies (i.e., 70 $\mu$M), could not be reached by simply diluting the concentrated free-base porphyrin (in 0.1 M KOH) into buffer H. These conditions were conducive to porphyrin aggregation in the absence of protein. However, the porphyrin solutions of required concentration were easily obtained by direct dilution of the concentrated porphyrin in 0.1 M KOH into buffer H containing ferrochelatase. Apparently, the protein environment allows complex formation before significant aggregation can occur. However, if more than 1 equiv of porphyrin is added, then we observe aggregation of the excess porphyrin. Porphyrin binding up to 1 equiv appears to be specific, i.e., at the high-affinity active site of wild-type ferrochelatase. Specific binding is further indicated by a plot of the absorbance of the ferrochelatase-bound porphyrin complex vs increasing concentrations of porphyrin. This plot can be nicely fitted assuming one binding site per ferrochelatase molecule. For several of these porphyrins, the dissociation constants ($K_D$) determined for porphyrin binding to ferrochelatase indicate strong binding. In the case of $H_2$(MesoP) (inset of Figure 3) and Ni(MesoP), the dissociation constants are in the micromolar range (5.0 and 4.3 $\mu$M, respectively) and in agreement with previous determinations using fluorescence spectroscopy (*4*). These values for the dissociation constants are also comparable to those for the mouse protein (2.2 $\mu$M) and for a known potent inhibitor, *N*-methyl-mesoporphyrin (Franco, R. et al., unpublished results). The fact that active site mutations influence the amount of endogenous porphyrin retained during isolation of the protein also provides supporting evidence for specific binding of porphyrins to the active site of ferrochelatase. In addition, the mutations influence the structure of the bound exogenous and endogenous porphyrin. Finally, specificity in the binding is further indicated by the effects on the vinyl-sensitive Raman lines of the porphyrin macrocycle. Ni(ProtoP) and probably $H_2$(ProtoP) show decreases in frequency of $\nu_2$ that are probably indicative of a specific orientation of the vinyl substituents for the wild-type ferrochelatase complex. For Ni(ProtoP), this is consistent with the change in intensity and perhaps frequency of the vinyl mode near 1633 cm$^{-1}$.

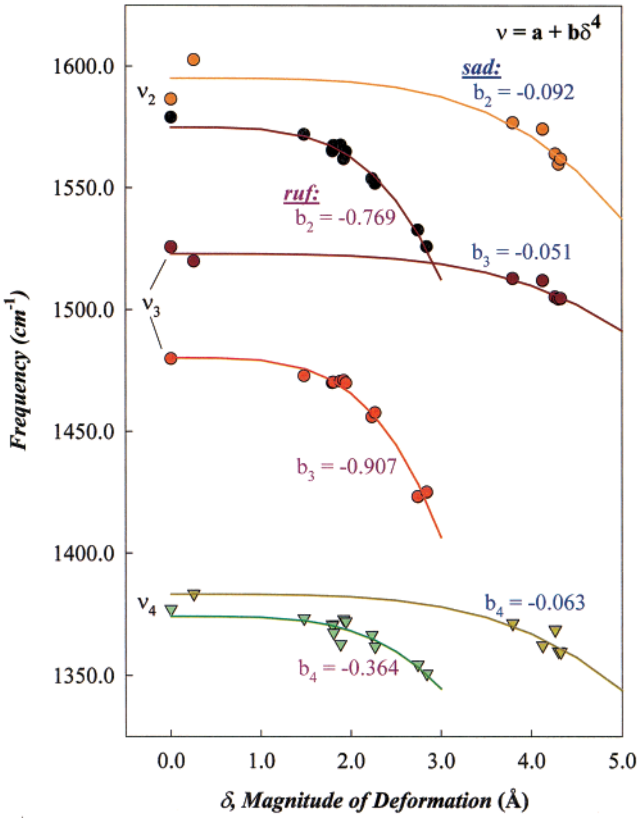

FIGURE 8: Relationships between Raman frequency and magnitude of deformation for series of predominantly ruffled (*ruf*) nickel porphyrins (Ni tetraalkyl(aryl)porphyrins) (*34*) and predominantly saddled (*sad*) porphyrins (Ni octaalkyl-tetraphenylporphyrins) (*36*). The curves are least-squares fits using the functional form $\nu = a + b\delta^4$, where $\delta$ is the magnitude of the deformation in Å. The intercept at zero deformation, *a*, and *b* are the fitting parameters. The values for *b* for $\nu_4$, $\nu_3$, and $\nu_2$ are given in the figure; those for *a* are 1374.3, 1480.3, and 1575.1 cm$^{-1}$ for ruffling and 1383.4, 1523.1, and 1595.2 cm$^{-1}$ for saddling, respectively.

The distortion of the porphyrin macrocycle that occurs upon binding to ferrochelatase might be thought to be small based on the small observed Raman shifts; however, this is not necessarily the case. Studies of model nonplanar Ni porphyrins undergoing different types of deformation, e.g., ruffling, doming, and saddling, indicate different sensitivities of the structure-sensitive Raman lines to the magnitude of the particular deformation (*27*). For example, the marker lines are much more sensitive to ruffling than to saddling. This is seen from the relationship between the Raman frequencies and the magnitudes of the *ruf* or *sad* deformations (determined using NSD) for two series of synthetic nonplanar Ni-porphyrin models (*34*, *36*) (Figure 8). The series of porphyrins with increasing *sad* deformation includes the octaalkyltetraphenylporphyrins (alkyl = methyl, ethyl, propyl) and the tetracycloalkyltetraphenylporphyrins with three-, four-, and five-membered alkyl chains fused to the $\beta$-pyrrole carbons of the porphyrin. The *ruf* porphyrin series includes the tetraalkylporphyrins in which the alkyl groups are methyl, ethyl, propyl, *n*-pentyl, isopropyl, cyclohexyl, apopinenyl, *tert*-butyl, adamantyl, and others. In general, the magnitude of the deformation increases as the bulkiness of the substituent increases. There is estimated to be between 5.8 ($\nu_4$) and 17.8 ($\nu_3$) times higher frequency sensitivity to ruffling than to saddling depending on the particular structure-sensitive line. This estimate is based on the ratio of the *b* parameters determined from least-squares fitting of the data in Figure 8 (see below). Thus, if the distortion were mostly *sad*, then the small frequency shifts that occur upon binding would indicate sizable saddling deformations, since the frequency depends so weakly on saddling. Another factor to be considered in evaluating the meaning of the shifts in the Raman lines is the observed nonlinear frequency dependence on the magnitude of these deformations. That is, the frequency dependence on deformation (slope) is initially small, but becomes stronger proportional to the third power of the deformation as the distortion increases, as can be seen in Figure 8. The frequency dependence is quite strong for deformations beyond 2 Å for ruffling and 3 Å for saddling.

Although the magnitudes and types of symmetric deformations making up the porphyrin distortion in ferrochelatase is still uncertain, it is clear from the resonance Raman data that some sort of distortion occurs and that this distortion is different for wild-type and the two mutant proteins. The distortion is evident from downshifts in the structure-sensitive line frequencies for the free base and the nickel porphyrins and for both MesoP and ProtoP. Thus, it is clear that the active site prefers at least a moderately nonplanar macrocycle.

How large are the porphyrin deformations in mouse ferrochelatase? We can obtain estimates of the deformations by assuming the downshifts alternatively arise from a pure ruffling or a pure saddling deformation, by using the relationships of Figure 8 to calculate the size of the deformation. For this purpose, it would be more accurate to use the downshifts in $\nu_{10}$, because of its higher sensitivity to deformation. However, $\nu_{10}$ is not observed in the model nonplanar porphyrin Raman data currently available, because this Raman line is not observed with Soret excitation for meso-substituted porphyrins. Instead, we have used the downshifts in $\nu_3$ to obtain an estimated of the extent of ruffling or saddling of ferrochelatase-bound porphyrin. For ruffling, using the 2.2-cm$^{-1}$ downshift for the Ni(MesoP)−ferrochelatase complex relative to the planar solution species, we obtained the ruffling displacement $\delta$ from $\Delta\nu_3 = \nu_3(0) - \nu_3(\delta) = -b_3\delta^4$ using $\Delta\nu_3 = 2.2$ cm$^{-1}$ and $b_3 = -0.907$, obtained from fitting this expression to the data in Figure 8. Thus, the ruffling deformation is $\delta_{\mathrm{ruf}} = (-\Delta\nu_3/b_3)^{1/4} = 1.2$ Å. A larger ruffling deformation is obtained from the larger downshift for Ni(ProtoP) binding to wild-type ferrochelatase. The downshift is also larger for the Ni(MesoP) complex with H207N mutant (3.5 cm$^{-1}$), giving a ruffling of 1.4 Å. The smaller downshift Ni(MesoP) complex with E287Q mutant (0.4 cm$^{-1}$) still gives a 0.8 Å ruffling. If the relationships for the Ni-porphyrin models (Figure 8) also held for the free-base porphyrins, then the 1.0 cm$^{-1}$ downshifts for $\nu_3$ of $H_2$(MesoP) would indicate a ruffling of 1.0 Å. On the other hand, if the shift is fully accounted for by saddling ($b_3 = -0.051$) instead of ruffling, then the estimated deformations are considerably larger. From the same downshifts for Ni(MesoP) binding, the magnitudes of the saddling $\delta_{\mathrm{sad}}$ would be 2.6, 2.9, and 1.7 Å, respectively, for the wild-type, H207N, and E287Q mutant proteins.

Clearly, the magnitude and possibly the relative contributions of the different types of symmetric deformations to the porphyrin distortion are altered by mutation of the conserved residues at the active site. For both Ni(MesoP) and Ni(ProtoP), binding to the H207N mutant causes larger decreases in frequency and presumably a larger distortion. However, the particular type of symmetric deformation affects the frequency dependence; thus, the frequency shifts could increase for the H207N mutant, because the types of deformations making up the distortion change, while the total magnitude of distortion might even decrease. Regardless, the Raman shifts suggest that histidine-207 may be more directly involved in catalysis than just binding the iron atom; histidine-207 may influence macrocycle conformation as well. Alternatively, it is possible that the mutation has a simple steric effect and that the unfavorable positioning of the introduced asparagine residue would cause the larger distortion or change in shape. Presumably, the free-base porphyrins show less distortion upon binding and also less influence of the mutation on porphyrin structure, possibly because the free-base porphyrins are less easily ruffled than the Ni porphyrins.

The model calculations for Ni(ProtoP) bound to the *B. subtilis* enzyme certainly suggest that the putative active site does not support a planar Ni porphyrin. The structures obtained are mainly ruffled, and the extent of the ruffling is consistent with our estimates of the ruffling based on the resonance Raman downshifts associated with binding to the enzyme. The ruffling varies from 0.4 to 2.0 Å (Figure 7), and for the two lowest energy structures, the ruffling is 1.3 and 1.5 Å (Figure 6). The calculated structures of Ni(ProtoP) are thus consistent with the 1.4 Å ruffling calculated from the Raman downshifts of $\nu_3$ for the Ni(ProtoP) complex with wild-type ferrochelatase (3.1 cm$^{-1}$). However, the ruffling deformation may be exaggerated by the use of the Ni derivative, because the small Ni ion favors the ruffling deformation (*40*).

The sublines of the Ni porphyrins bound to H207N mutant suggest that the site is more heterogeneous than for wild-type protein, since ruffled and near planar conformers coexist. Although the ruffling for the H207N mutant is not as great as for the solution ruffled conformer, it is greater than for the ruffled conformer in ferrochelatase. Again, these statements are based on the assumption that ruffling causes the frequency difference. Although unlikely, large differences in other types of deformation might account for the frequency differences in marker lines.

For the E287Q mutant, the mutation has a large effect on the affinity for free-base porphyrin. Specifically, free-base porphyrin remains bound to about 15% of the mutant protein during preparation, much more than for wild-type ferrochelatase. Furthermore, the endogenous porphyrin is not displaced by nickel porphyrins that bind to wild-type with an affinity high enough to give almost complete complex formation at 1 equiv or higher of added porphyrin (Figures 1D and 2D). Finally, the mode of binding of endogenous porphyrin to wild-type and E287Q mutant differs, since the resonance Raman spectra of the endogenously bound porphyrin of wild-type and the E287Q mutant differ significantly (Figure 5, B and E).

The strong influence of the mutation of glutamic acid-287 on the porphyrin binding to ferrochelatase (Figure 6A) suggests that it may play a part in the substrate-binding site of the enzyme. Further, the unusual resonance Raman spectra of the endogenous porphyrin of ferrochelatase (Figure 5B) and the E287Q mutant (Figure 5E) suggest that free-base porphyrin interacts strongly with the active site, and glutamic acid-287 in particular, to give a porphyrin species that is uniquely different from the solution models (e.g., Figure 5A). From Figure 6B, it is clear that for some orientations of the substrate, a propionate of the porphyrin could interact strongly with the neutral glutamine-287 of the mutant, but only weakly with the negative glutamic acid residue of the wild-type. However, presently, the proposed direct catalytic role of E287 (*18*) should not be ruled out.

To date, we have no definitive interpretation of the drastically altered spectra of the endogenous porphyrin bound to wild-type and E287Q ferrochelatase. The large upshifts in frequency of the structure-sensitive lines could indicate a large distortion of the macrocycle. However, the observed upshifts in frequency would not be expected for a ruffled or saddled porphyrin. A specific interaction with the pyrrole protons might cause such frequency shifts. Clearly, a better understanding of the origin of these shifts, which occur for a fraction of the bound porphyrin, might further elucidate the catalytic mechanism, but better porphyrin models are needed to reliably interpret these data.

Currently, resonance Raman studies of *N*-methylporphyrin binding to mouse ferrochelatase and its mutants are underway. These will be coupled with molecular simulations of porphyrin bound at the now known location and orientation of the porphyrin at the active site of *B. subtilis* ferrochelatase (Al-Karadaghi, S., personal communication.). Resonance Raman spectra of ferrochelatase complexes in the low-frequency region may also provide additional information about the distortion and specific interactions between the protein and peripheral substituents of the porphyrin substrate.

Other authors (*24*, *48*) have observed very small shifts in the structure-sensitive Raman lines upon binding mesoporphyrin to yeast ferrochelatase. However, for the yeast protein, no change in the frequency of $\nu_4$ and $\nu_{10}$ is observed, and $\nu_3$ actually increases by 1 $cm^{-1}$ (*48*). In contrast, for the mouse protein, a ~1 $cm^{-1}$ decrease in frequency is observed for $\nu_3$ and $\nu_{10}$, indicating as much as 1 Å ruffling deformation. Finally, we have not yet investigated effects of metal substrate binding on the out-of-plane conformation of the porphyrins. Blackwood et al. (*48*) have used $Hg^{2+}$ as a competitive inhibitor to freeze the substrate porphyrin in an activated-state conformation and have observed significant Raman frequency shifts. However, our own observations of $Hg^{2+}$ titrations of murine ferrochelatase followed by UV−vis and CD spectroscopies indicate that the cluster is destroyed at Hg/protein ratios as low as 0.25 and that the protein starts getting irreversibly denatured at Hg/protein ratios of 1.0 (data not shown); thus useful comparisons with these resonance Raman studies of the yeast protein cannot be made at this time.

## REFERENCES

1. Ferreira, G. C., Franco, R., Lloyd, S. G., Moura, I., Moura, J. J. G., and Huynh, B. H. (1995) *J. Bioenerg. Biomemb. 27*, 221−229.
2. Dailey, H. A. (1996) in *Mechanisms of Metallocenter Assembly* (Hausinger, R. P., Eichorn, G. L., and Marzelli, L. G., Eds.), VCH: New York, 77−98.
3. Harbin, B. M., and Dailey, H. A. (1985) *Biochemistry 24*, 366−70.
4. Dailey, H. A. (1990) in *Biosynthesis of Heme and Chlorophylls* (Dailey, H. A., Ed.), McGrawHill Publishing, New York.
5. Nakahigashi, K., Nishimura, K., Miyamoto, K., and Inokuchi, H. (1991) *Proc. Natl. Acad. Sci. U.S.A. 88*, 10520−4.
6. Frustaci, J. M., and O'Brian, M. R. (1992) *J. Bacteriol. 174*, 4223−9.
7. Kanazireva, E., and Biel, A. J. (1996) *Gene (Amsterdam) 170*, 149−150.
8. Labbe-Bois, R. (1990) *J. Biol. Chem. 265*, 7278−83.
9. Miyamoto, K., Tanaka, R., Teramoto, H., Masuda, T., Tsuji, H., and Inokuchi, H. (1994) *Plant Physiol. 105*, 769−70.
10. Day, A. L., Parsons, B. M., and Dailey, H. A. (1998) *Arch. Biochem. Biophys. 359*, 160−9.
11. Taketani, S., Nakahashi, Y., Osumi, T., and Tokunaga, R. (1990) *J. Biol. Chem. 265*, 19377−80.
12. Brenner, D. A., and Frasier, F. (1991) *Proc. Natl. Acad. Sci. U.S.A. 88*, 849−53.
13. Shibuya, H., Nonneman, D., Tamassia, M., Allphin, O. L., and Johnson, G. S. (1995) *Biochim. Biophys. Acta 1231*, 117−20.
14. Nakahashi, Y., Taketani, S., Okuda, M., Inoue, K., and Tokunaga, R. (1990) *Biochem. Biophys. Res. Commun. 173*, 748−55.
15. Al-Karadaghi, S., Hansson, M., Nikonov, S., Jonsson, B., and Hederstedt, L. (1997) *Structure (London) 5*, 1501−1510.
16. Kohno, H., Okuda, M., Furukawa, T., Tokunaga, R., and Taketani, S. (1994) *Biochim. Biophys. Acta 1209*, 95−100.
17. Franco, R., Moura, J. J. G., Moura, I., Lloyd, S. G., Huynh, B. H., Forbes, W. S., and Ferreira, G. C. (1995) *J. Biol. Chem. 270*, 26352−26357.
18. Gora, M., Grzybowska, E., Rytka, J., and Labbe-Bois, R. (1996) *J. Biol. Chem. 271*, 11810−11816.
19. Ferreira, G. C., Franco, R., Lloyd, S. G., Pereira, A. S., Moura, I., Moura, J. J. G., and Huynh, B. H. (1994) *J. Biol. Chem. 269*, 7062−7065.
20. Dailey, H. A., Finnegan, M. G., and Johnson, M. K. (1994) *Biochemistry 33*, 403−407.
21. Dailey, H. A., and Fleming, J. E. (1983) *J. Biol. Chem. 258*, 11453−9.
22. Cochran, A. G., and Schultz, P. G. (1990) *Science 249*, 781−783.
23. Romesberg, F. E., Santarsiero, B. D., Spiller, B., Yin, J., Barnes, D., Schultz, P. G., and Stevens, R. C. (1998) *Biochemistry 37*, 14404−9.
24. Blackwood, M. E., Jr., Rush, T. S., III, Romesberg, F., Schultz, P. G., and Spiro, T. G. (1998) *Biochemistry 37*, 779−782.
25. Sanger, F., Nicklen, S., and Coulson, A. R. (1977) *Proc. Natl. Acad. Sci. U.S.A. 74*, 5463−5467.
26. Abbas, A., and Labbe-Bois, R. (1993) *J. Biol. Chem. 268*, 8541−8546.
27. Song, X. Z., Jentzen, W., Jia, S. L., Jaquinod, L., Nurco, D. J., Medforth, C. J., Smith, K. M., and Shelnutt, J. A. (1996) *J. Am. Chem. Soc. 118*, 12975−12988.
28. Mayo, S. L., Olafson, B. D., and Goddard, W. A. (1990) *J. Phys. Chem. 94*, 8897−8909.
29. Song, X. Z., Jaquinod, L., Jentzen, W., Nurco, D. J., Jia, S. L., Khoury, R. G., Ma, J. G., Medforth, C. J., Smith, K. M., and Shelnutt, J. A. (1998) *Inorg. Chem. 37*, 2009−2019.
30. Song, X. Z., Jentzen, W., Jaquinod, L., Khoury, R. G., Medforth, C. J., Jia, S. L., Ma, J. G., Smith, K. M., and Shelnutt, J. A. (1998) *Inorg. Chem. 37*, 2117−2128.
31. Sparks, L. D., Medforth, C. J., Park, M. S., Chamberlain, J. R., Ondrias, M. R., Senge, M. O., Smith, K. M., and Shelnutt, J. A. (1993) *J. Am. Chem. Soc. 115*, 581−592.
32. Sparks, L. D., Chamberlain, J. R., Hsu, P., Ondrias, M. R., Swanson, B. A., Demontellano, P. R. O., and Shelnutt, J. A. (1993) *Inorg. Chem. 32*, 3153−3161.
33. Sparks, L. D., Anderson, K. K., Medforth, C. J., Smith, K. M., and Shelnutt, J. A. (1994) *Inorg. Chem. 33*, 2297−2302.
34. Jentzen, W., Simpson, M. C., Hobbs, J. D., Song, X., Ema, T., Nelson, N. Y., Medforth, C. J., Smith, K. M., Veyrat, M., Mazzanti, M., Ramasseul, R., Marchon, J. C., Takeuchi, T., Goddard, W. A., III, and Shelnutt, J. A. (1995) *J. Am. Chem. Soc. 117*, 11085−11097.
35. Shelnutt, J. A., Majumder, S. A., Sparks, L. D., Hobbs, J. D., Medforth, C. J., Senge, M. O., Smith, K. M., Miura, M., Luo, L., and Quirke, J. M. E. (1992) *J. Raman Spectrosc. 23*, 523−529.
36. Shelnutt, J. A., Medforth, C. J., Berber, M. D., Barkigia, K. M., and Smith, K. M. (1991) *J. Am. Chem. Soc. 113*, 4077−4087.
37. Rappe, A. K., Goddard, W. A., III (1991) *J. Phys. Chem. 95*, 3358−3363.

38. Jentzen, W., Song, X., and Shelnutt, J. A. (1996) *Biophys. J. 70*, A153.
39. Jentzen, W., Ma, J. G., and Shelnutt, J. A. (1998) *Biophys. J. 74*, 753−63.
40. Shelnutt, J. A., Song, X. Z., Ma, J. G., Jia, S. L., Jentzen, W., and Medforth, C. J. (1998) *Chem. Soc. Rev. 27*, 31−41.
41. Jentzen, W., Song, X. Z., and Shelnutt, J. A. (1997) *J. Phys. Chem. B 101*, 1684−1699.
42. Alden, R. G., Ondrias, M. R., and Shelnutt, J. A. (1990) *J. Am. Chem. Soc. 112*, 691−697.
43. Alden, R. G., Crawford, B. A., Doolen, R., Ondrias, M. R., and Shelnutt, J. A. (1989) *J. Am. Chem. Soc. 111*, 2070−2072.
44. Anderson, K. K., Hobbs, J. D., Luo, L., Stanley, K. D., Quirke, J. M. E., and Shelnutt, J. A. (1993) *J. Am. Chem. Soc. 115*, 12346−12352.
45. Brennan, T. D., Scheidt, W. R., and Shelnutt, J. A. (1988) *J. Am. Chem. Soc. 110*, 3919−3924.
46. Meyer, E. F. (1972) *Acta Crystallogr. B28*, 2162−2167.
47. Cullen, D. L., and Meyer, J., E. F. (1974) *J. Am. Chem. Soc. 96*, 2095−2102.
48. Blackwood, M. E., Rush, T. S., Medlock, A., Dailey, H. A., and Spiro, T. G. (1997) *J. Am. Chem. Soc. 119*, 12170−12174.

BI991346T